GEOPHYSICAL RESEARCH LETTERS, VOL. 27, NO. 1, PAGES 41-44, JANUARY 1, 2000

Atmospheric gravity wave signatures in the infrared hydroxyl OH airglow

H. U. Frey, S. B. Mende, J. F. Arens

Space Sciences Laboratory, University of California, Berkeley

P. R. McCullough, G. R. Swenson

University of Illinois, Urbana

Abstract. Atmospheric gravity wave induced airglow fluctuations of the hydroxyl OH Meinel and other bands are routinely observed using CCD imagers operating in the near infrared wavelength region. Farther into the infrared, the intensity of the OH emissions is much greater. Recently, a new IR imaging camera was modified for infrared viewing of the night sky with approximately 1 steradian field of view. The filter had a center wavelength of 1467 nm and a bandwidth of 177 nm to include components of the OH ($\Delta v = 2$) band. The images show good signal-to-noise ratios of 180 with 10 second exposures. Cross-spectral and wavelet analysis were used to obtain spatial and temporal information about observed airglow fluctuations, and horizontal wavelengths and wave periods as short as 3.7 km and 3 min, respectively, were determined.

1. Introduction

Atmospheric gravity waves (AGW) created in the lower atmosphere and propagating in the mesosphere and lower-thermosphere critically influence the energetics and dynamics of the region by momentum transfer, and to a lesser degree by direct energy dissipation. An observable effect of gravity waves is airglow modulation caused by density/temperature variations of the wave fields. Swenson and Gardner [1998] have developed and validated the relationship between OH intensity perturbations and the AGW amplitudes. This has been extended to calculations of the vertical flux of wave energy and the horizontal momentum carried by the waves through the airglow layer [*Swenson and Liu,* 1998].

Atmospheric gravity waves have been observed in airglow images for many years (for a review see [*Taylor,* 1997]). During recent years, CCD cameras became the instruments of choice for airglow imaging; however, their sensitivity cutoff around 900 nm enabled observations in the visible and near-infrared region only.

One of the most important airglow emissions comes from the hydroxyl OH. Its importance lies in the photochemistry of ozone creation from atomic oxygen and its destruction by hydrogen producing the OH infrared emission [*Good,* 1976]. The emission peaks at 87 ± 3 km and can be used to determine the atomic oxygen altitude profile [*Ulwick et al.,* 1987] and the mesopause temperature [*Mulligan et al.,* 1995].

Previous ground-based airglow observations mostly used emissions from oxygen (OI at 557.7 nm and 630 nm) or OH (8,3 transitions at 731-733 nm [see e.g. *Swenson et al.,* 1990; *Taylor and Garcia,* 1995]) in the visible and NIR range. However, the OH emissions in the infrared (longer than 1 μm) are much brighter [*Turnbull and Lowe,* 1983].

A disadvantage of imagers operating in the 1-2 μm region is the necessity of cooling the detector in order to reduce the instrument noise. If these features could be observed from a nadir viewing spacecraft, water vapor and CO_2 absorption bands offer a major advantage to eliminate albedo effects for other rotational features in these bands (which are not observable from the ground). Such observations could provide a global mapping of gravity wave propagation which is necessary for global scale models of the mesosphere and lower-thermosphere.

This paper describes the ground-based observation of gravity wave modulated variations in OH airglow images in the 1.4-1.5 μm infrared region.

2. Instrumentation and data analysis

An imaging camera using a NICMOS3 256x256 array, which was originally developed for astronomical applications, was modified by incorporating a filter and a telecentric wide field of view lens suitable for infrared viewing of the night sky [*Meixner et al.,* 1999]. With liquid nitrogen cooling, the array's dark current of 1 e^-/s is negligible compared to the brightness of the night sky.

The star background was used for the geometrical calibration. The field of view was 46°x46°, corresponding to 74x74 km^2 at 87 km altitude.

Many different filters with center wavelengths between 985 nm and 2275 nm were used. This report concentrates only on data obtained with the filter at 1467 nm wavelength and a bandwidth of 177 nm. This spectral band pass includes all the (2,0) r- and q-branches of OH and just reaches the (3,1) transition region at the longer wavelength [*Sivjee and Walterscheid,* 1994].

Paper number 1999GL010695.
0094-8276/00/1999GL010695$05.00

The imager was operated during two clear nights on March 20 and 21, 1998, at the Mt. Laguna observatory in Southern California (243.6° Longitude, 32.8° Latitude). Image sequences with exposure times between 1 s and 50 s and repetition times between 20 s and 60 s were acquired. This investigation concentrates on a continuous 100 min time series with 20 s exposures every 30 s (200 images) recorded on March 21 after 2303 local time (PST). The images were flat-fielded and salt-and-pepper noise and stars were removed.

Many different techniques have been used to obtain information on the gravity waves from imager data, like spectral analysis (see e.g. [*Taylor and Garcia,* 1995]), time differencing (see e.g. [*Swenson and Mende,* 1994]), or cross-correlation (see e.g. [*Fagundes et al.,* 1995]). Here we use cross-spectral analysis for the spatial and wavelet analysis for the temporal characterization.

The cross spectrum $\Gamma_{12}(f)$ of two time series $u_1(t)$ and $u_2(t)$ is

$$\Gamma_{12} = \frac{\langle U_1^* U_2 \rangle}{\langle |U_1|^2 \rangle^{1/2} \langle |U_2|^2 \rangle^{1/2}} = A_{12} \exp^{i\Phi_{12}} \qquad (1)$$

with the Fourier transforms U_1 and U_2 of u_1 and u_2 [see e.g. *Jenkins and Watts,* 1968; *Bendat and Piersol,* 1993]. The asterisk denotes the complex conjugate. Here we calculate the two-dimensional spatial Fourier transform with respect to x,y in our images and average over a certain time period, denoted by the delimiters $\langle\rangle$. The complex cross spectrum Γ_{12} may also be written as the product of a magnitude term A_{12} and the phase term with the phase Φ_{12}. The quantity A_{12}^2 is often referred to as the squared cross-coherency and quantifies the degree of correlation between the amplitude of a signal in one time series with the same signal in the other time series.

Wavelet analysis is becoming a common tool for analyzing localized variations of power within a time series (see e.g. [*Chan,* 1995]). By decomposing a time series into time-frequency space, one is able to determine both the dominant modes of variability and how those modes vary in time (see e.g. [*Torrence and Compo,* 1998]). In this regard wavelet analysis is superior to Fourier analysis as the latter can only provide global frequency information. Furthermore, wavelet analysis does not contain the inaccuracies of the windowed Fourier transform [*Torrence and Compo,* 1998].

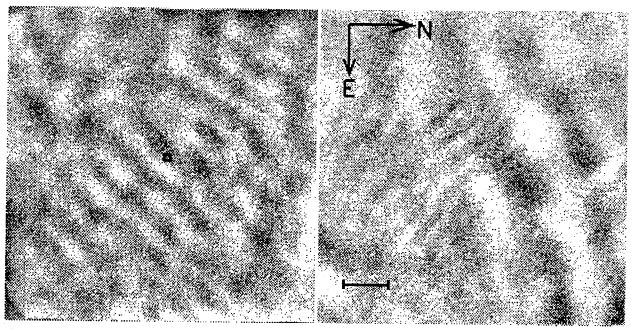

Figure 1. Examples for gravity wave modulated OH airglow. The left image shows a regular pattern with 7.5 km horizontal wavelength filling almost the entire field of view. The black square marks the region used for the wavelet analysis. The right image shows two almost perpendicular wave fronts with 3.7 km and 16.5 km horizontal wavelength, respectively. The N-E directions are given. The field of view is 46° x 46°. The scale at the bottom shows 10 km at 87 km altitude.

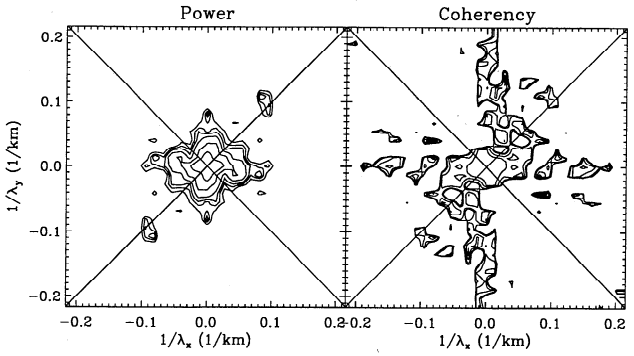

Figure 2. Results of the cross-spectral analysis. The left panel shows the averaged power in the images taken between 32 min and 36 min of the sequence. The axes show the horizontal wavenumber. The right panel shows the cross-coherency between images taken 1 min apart with contours at coherency of 0.75, 0.85, and 0.95. The diagonal lines were drawn to guide the eye.

3. Observations

Several series of images with and without illumination were used to determine the signal to noise ratio for the instrument. With 0.1 s exposures, signal to noise ratios of 16 could be reached, and for 10 s integration time the ratio was 180 at 1.4 μm.

Figure 1 shows examples of OH airglow images. For this presentation only, the images were high-pass filtered and contain only horizontal wavelengths shorter than 25 km. The left part of Figure 1 shows an image taken 33 min after the start of the 100 min series and contains a regular wave pattern with 7.5 km horizontal wavelength. The right part will be discussed later.

The series of 200 images was divided into groups of 8 images. The left panel of Figure 2 shows the time averaged power in the group of images taken between t_{11}=32 min and t_{12}=35.5 min with respect to the horizontal wavenumber. The two peaks at wavenumber of about [0.1 km^{-1}, 0.1 km^{-1}] and [-0.1 km^{-1}, -0.1 km^{-1}] show the power in the short wavelength patter of Figure 1, left. The least square fitted position of the maximum is at [0.094 km^{-1}, 0.095 km^{-1}] and represents a horizontal wavelength of 7.5 $\pm$ 0.3 km. This pattern will later be shown to travel at 39 m/s northwest and to have a period of 3 minutes. The broad structure in the center of the two-dimensional spatial power spectrum repre-

sents image structures with wavelengths longer than 20 km, however no particular peak could be isolated.

For each group of 8 images the cross-spectrum was calculated with the group of images taken 30 s, 1 min, 2 min, and 4 min later. The result for the image group taken at t_{11}=32 min with images taken 1 min later is shown in the right panel of Figure 2 with the cross-coherency given with contours at 0.8, 0.85, 0.9, and 0.95. Several points of high coherency are visible, but only the ones with high spectral power are relevant. The coherency at wavenumber [0.094 km^{-1}, 0.095 km^{-1}] and [-0.094 km^{-1}, -0.095 km^{-1}] is 0.97 with an error of 0.02 [*Bendat and Piersol,* 1993]. At this point of high spectral power the cross-coherency for all different groups and time differences changes slightly but is always greater than 0.95. For comparison, the respective number for the cross spectrum at wavenumber [0.094 km^{-1}, -0.095 km^{-1}] where the spectral power is a factor of 40 smaller, is a coherency of 0.17 ± 0.17. This corresponds to no significant coherency.

The cross spectral analysis also provides the phase difference which in this particular example of 1 min time difference at the location of the peak in the power spectrum is -112°± 2° (not shown here) . The cross spectral analysis with images taken 30 s apart gives a phase difference of -56°± 2°. Much longer time differences like 4 min can not be used to reliably determine the phase difference because it would get greater than -180° and subject to aliasing.

The horizontal wavenumber and phase can then be used to determine the velocity of the wave and to resolve the 180° ambiguity in the cross-coherency. A phase shift of 2π for a peak at (k_x, k_y) in the 2-D cross spectrum corresponds to a spatial shift of one wavelength. Knowing the distance the phase front traveled, and the time between the images, the horizontal phase velocity of the wave can be determined. In our presentation of the cross spectrum (Equation 1) a phase difference of -56° represents a wave moving towards the north-west. The horizontal phase speed of the wave is 56/360*7500/30=39 ± 2 m/s. This speed is well within the 20 to 100 m/s range of horizontal phase speeds observed for longer horizontal wavelengths of 15-40 km [*Gardner and Taylor,* 1998].

In order to determine temporal properties of the airglow fluctuations we used wavelet analysis. We selected a region in the center of our images (2x2 pixels) and constructed the time series of pixel content (airglow intensity). Then we linearly detrended the data and applied the Morlet and Paul wavelets to our time series (Figure 3). Both wavelet analyses show fluctuations of 2-3 min period between 28 and 38 min of the time series. This is the signature of the 7.5 km short wavelength modulation. At the time of the previously discussed cross-spectral analysis the observed period is 3 ± 0.5 min. The Morlet wavelet provides a better localization in observed frequency. The Paul wavelet on the other hand provides a better localization in time [*Torrence and Compo,* 1998]. Other regions of 2x2 pixels in the central part of the images showed very similar results.

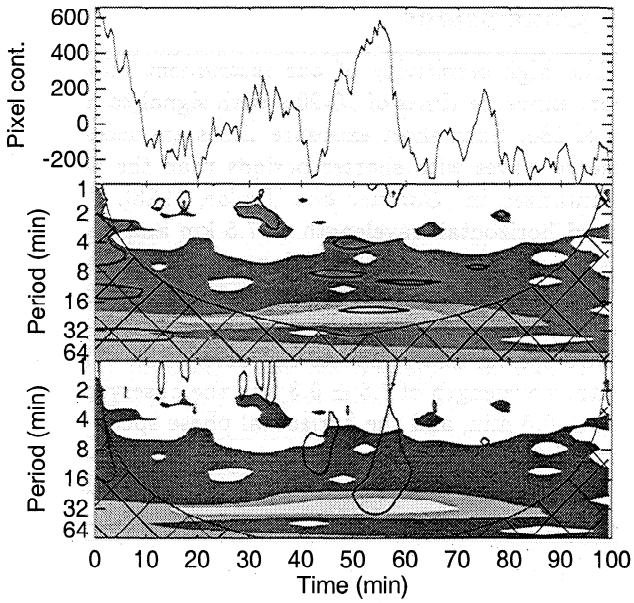

Figure 3. Result of the wavelet analysis. The top panel gives the pixel content in the 2x2 region. The middle and bottom panels are the results of the Morlet and Paul wavelet analysis. The observed wave period is given in minutes. The black lines enclose regions of greater than 90 % confidence. Results in the cross hatched regions should be ignored due to edge effects.

After 40 min the characteristics of the wave patterns changed to longer horizontal wavelengths of 11 km and later after 50 min to 33 km (not shown here). These structures can be seen in the wavelet analysis with observed periods around 4-5 min and 16-18 min, respectively. This may prove to be an important and not unusual feature of these types of measurements as already [*Taylor et al.,* 1998] mention a wavelength "splitting" and as a "doubling" seems to be possible as well. There are some more structures with much longer periods, however the significance of these structures is questionable due to edge effects.

The right image in Figure 1 of 10 s exposure time from March 20, 1926 LT contains two wave patterns, with 3.7 ± 0.4 km and 16.5 ± 1.0 km horizontal wavelength, aligned almost perpendicular to each other. This pattern very much resembles the observations of breaking waves [*Swenson and Mende,* 1994; *Hecht et al.,* 1997]. The longer wavelength pattern moved to the north-west at 29 ± 5 m/s. The short wavelength pattern moved towards the south-west with the same horizontal phase speed of 29 ± 5 m/s. Unfortunately, this particular image sequence was only 4 min long and we cannot directly determine the period and how long this pattern persisted. We can only estimate the period from the observed horizontal phase velocity and horizontal wavelength as 2.1 min and 9.5 min, respectively.

4. Conclusions

The high sensitivity of our instrument allowed for short exposure times of 10-20 s with signal to noise ratio of 180. Such short exposure times are necessary to observe waves with shorter periods than the 5-10 min summarized in [*Gardner and Taylor,* 1998]. The observed horizontal wavelength of 7.5 km and periods of 2-3 min agree with extrapolations of their results.

The combination of cross-spectral and wavelet analysis enabled a complete determination of the gravity wave's spatial and temporal characteristics. The horizontal wavelength of 7.5 $\pm$ 0.3 km, the observed period of 3 $\pm$ 0.5 min, and the horizontal phase speed of 39 $\pm$ 2 ms^{-1} fit very well together.

We showed one example with a very short horizontal wavelength of 3.7 km, much shorter than the data summarized in [*Gardner and Taylor,* 1998], and also shorter than the "breaking wave" reported in [*Swenson and Mende,* 1994]. Future ground-based measurements should be performed at facilities where the winds can be measured simultaneously in order to gather intrinsic wave information and distinguish between true gravity wave parameters and Doppler shifted values [*Gardner and Taylor,* 1998]. These measurements would help to resolve the question, why periods of 2-3 min were observed. Such short period waves should not exist since the Brunt Vaisala frequency predicts periods of more than $\approx$ 5 min and the observation may well be the result of Doppler shifting.

Acknowledgments. We appreciate the assistance of the staff of the Mt. Laguna Observatory. Margaret Meixner built the infrared camera. PRM's research is funded in part by the Sloan Foundation and the Research Corporation. Wavelet software was provided by C. Torrence and G. Compo. HUF appreciates discussion with G. Delory.

References

Chan, Y. T., *Wavelet basics*, Kluwer, Boston, 1995.

Bendat, J. S. and A. G. Piersol, *Engineering applications of correlation and spectral analysis,* Wiley, New York, 1993.

Fagundes, P. R., H. Takahashi, Y. Sahai, and D. Gobbi, Observations of gravity waves from multispectral mesospheric nightglow emissions observed at 23 degrees S, *J. Atmos. Terr. Phys., 57,* 395–405, 1995.

Hecht, J. H., R. L. Walterscheid, D. C. Fritts, J. R. Isler, D. C. Senft, C. S. Gardner and S. J. Franke, Wave breaking signatures in OH airglow and sodium densities and temperatures. 1. Airglow imaging, Na lidar, and MF radar observations, *J. Geophys. Res., 102,* 6655–6668, 1997.

Gardner, C. S. and M. J. Taylor, Observational limits for lidar, radar, and airglow imager measurements of gravity wave parameters, *J. Geophys. Res., 103,* 6427–6437, 1998.

Good, R. E., Determination of atomic oxygen density from rocket borne measurement of hydroxyl airglow, *Planetary and Space Science, 24,* 389-95, 1976.

Jenkins, G. M. and D. G. Watts, *Spectral analysis and its applications,* Holden-Day, San Francisco, 1968.

Meixner, M, R. C. Young Owl, and R. Leach, NIRIM: A Dual Purpose Near Infrared (0.76-2.5 μm) Imaging Camera for Wide Field and High Resolution Imaging, in press in *Publ. Astronomical Soc. Pacific,* 1999.

Mulligan, F. J., D. F. Horgan, J. G. Galligan, and E. M. Griffin, Mesopause temperatures and integrated band brightnesses calculated from airglow OH emissions recorded at Maynooth (53.2 degrees N, 6.4 degrees W) during 1993, *J. Atmos. Terr. Phys., 57,* 1623-1637, 1995.

Sivjee, G. G., and R. L.Walterscheid, Six-hour zonally symmetric tidal oscillations of the winter mesopause over the South Pole station, *Planet. Space Sci., 42,* 447-453, 1994.

Swenson, G. R., S. B. Mende, and S. P. Geller, Fabry-Perot imaging observations of OH(8-3): rotational temperatures and gravity waves, *J. Geophys. Res., 95,* 12251-12263, 1990.

Swenson, G. R. and S. B. Mende, OH emission and gravity waves (including a breaking wave) in all-sky imagery from Bear Lake, UT, *Geophys. Res. Lett., 21,* 2239–2242, 1994.

Swenson, G. R. and A. Z. Liu, A model for calculating acoustic gravity wave energy and momentum flux in the mesosphere from OH airglow, *Geophys. Res. Lett., 25,* 477-480, 1998.

Swenson, G. R. and C. S. Gardner, Analytic models for the responses of the mesospheric OH and Na layers to atmospheric gravity waves, *J. Geophys. Res., 103,* 6271-6294, 1998.

Taylor, M. J., A review of advances in imaging techniques for measuring short period gravity waves in the mesosphere and lower thermosphere, *Adv. Space Res., 19,* 667–676, 1997.

Taylor, M. J. and F. J. Garcia, A two-dimensional spectral analysis of short period gravity waves imaged in the OI(557.7 nm) and near infra red OH nightglow emissions over Arecibo, Puerto Rico, *Geophys. Res. Lett., 22,* 2473–2476, 1995.

Taylor, M. J., S. H. Seo, T. Nakamura, T. Tsuda, H. Fukunishi, and Y. Takahashi, Long base-line measurements of short-period mesospheric gravity waves during the SEEK campaign, *Geophys. Res. Lett., 25,* 1797–1800, 1998.

Torrence, V. and G. P. Compo, A practical guide to wavelet analysis, *Bull. Amer. Meteor. Soc., 79,* 61–78, 1998.

Turnbull, D. N. and R. P. Lowe, Vibrational population distribution in the hydroxyl nightglow, *Can. J. Phys., 61,* 244–250, 1983.

Ulwick, J. C., K. D. Baker, D. J. Baker, A. J. Steed, W. R. Pendleton, K. Grossmann, and H. G. Bruckelmann, Mesospheric minor species determinations from rocket and ground-based i.r. measurements, *J. Atmos. Terr. Phys., 49,* 855-862, 1987.

J. F. Arens, H. U. Frey, S. B. Mende, Space Sciences Laboratory, University of California, Berkeley, CA 94720-7450 (e-mail: hfrey@ssl.berkeley.edu.

P. R. McCullough, G. R. Swenson, University of Illinois, Urbana, IL 61801 (email: pmcc@astro.uiuc.edu.

(Received June 8, 1999; revised November 8,1999; accepted November 16,1999.)